CHINESE OPTICS LETTERS

Vol. 21, No. 2 | February 2023

Metasurfaces enabled dual-wavelength decoupling of near-field and far-field encoding

Jun Liu (刘 俊)[1], Xiaoshu Zhu (朱效舒)[1], Juanzi He (贺涓子)[1], Yifan Zhou (周怡帆)[1], Mingqian Shi (石鸣谦)[1], Zhaofu Qin (覃赵福)[1], Shuming Wang (王漱明)[1,2,3*], and Zhenlin Wang (王振林)[1,2]

[1] National Laboratory of Solid State Microstructures, School of Physics, Nanjing University, Nanjing 210093, China

[2] Key Laboratory of Intelligent Optical Sensing and Manipulation, Ministry of Education, Nanjing University, Nanjing 210093, China

[3] Collaborative Innovation Center of Advanced Microstructures, Nanjing 210093, China

*Corresponding author: wangshuming@nju.edu.cn

Received May 10, 2022 | Accepted August 30, 2022 | Posted Online October 14, 2022

The metasurface is a platform with a small footprint and abundant functionalities. With propagation phase and geometric phase, polarization multiplexing is possible. However, different response behaviors of propagation phase and geometric phase to wavelength have not been fully employed to widen the capabilities of metasurfaces. Here, we theoretically demonstrate that metasurfaces can achieve near-field and far-field decoupling with the same polarization at two wavelengths. First, we found a set of pillars whose propagation phase difference between two wavelengths covers the full range of 2π. Then, by rotating pillars to control the geometric phase, the phase at both wavelengths can cover the full range of 2π. Finally, by means of interference principle, arbitrary independent coding for the near field and far field of dual wavelengths is realized. In addition, when the far-field function is focusing, the focused spot is close to the diffraction limit, and, when the NA of the lens is very small, the final output focal length is four times of initial input focal length. This work circumvents the strong wavelength-dependent limitation of planar devices and paves the way toward designing multi-wavelength and multi-functional metadevices for scenarios such as AR applications, fluorescence microscopy, and stimulated emission depletion microscopy.

Keywords: metasurfaces; multiplexing; dual-wavelength; decoupling.

DOI: 10.3788/COL202321.023602

1. Introduction

Metasurfaces[1], which are made of micro-optical antennas with versatile shapes and arrangements, circumvent the fabrication problems with one dimension reduced to the subwavelength scale, without sacrificing powerful functionalities. The research fields of metasurfaces can be roughly divided into two categories: classical and quantum domains. In the classical domain, the invisible cloak carpet[2], metalens[3,4], holography[5], nonlinear optics[6], and so on have been demonstrated. On the other hand, in the quantum domain, researchers have developed highly integrated quantum optical elements, ranging from quantum sources based on metalens[7], quantum manipulation[8–10] and applications[11–14], quantum vacuum engineering of quantum emitters[15–17], and so on. Interested readers can refer to several comprehensive reviews published recently[18,19].

Among all, researchers care about the abundant capabilities embedded in only one metasurface sample. Degrees of freedom of light, such as wavelength[20–22], incident[23–25] or output directions[26], orbital angular momentum[27–29], and polarizations[30–32], have been explored for realizing multiple functionalities. The state of light passing through metasurfaces is dependent on the degrees of freedom of incident photons. Combining the propagation phase and geometric phase of metasurfaces, independent and arbitrary phase can be encoded into orthogonal polarization bases[32,33]. Furthermore, relying on the subwavelength-scale pixels of metasurfaces and the interference principle, the complete decoupling of near- and far-field patterns for orthogonal polarization bases is possible[30]. Meanwhile, independent far-field patterns encoded into two wavelengths have also been confirmed feasible[34]. However, near- and far-field patterns decoupled completely for two wavelengths simultaneously have yet to be demonstrated.

In this paper, we utilize the different dispersion properties of propagation phase and geometric phase to achieve 2π full coverage of phases of the same polarization at two wavelengths. We firstly find the pillars that satisfy different propagation phase difference, which covers the 2π full range, then use the geometric phase being indistinguishable for different wavelengths; and the total phase with 2π full coverage, which equals propagation phase plus geometric phase, can be achieved just by rotating the pillars. Finally, the interference principle can be used to realize any independent regulation in the near field and far field for dual wavelengths. As shown in Fig. 1, the near-field pattern and far-field holography for two wavelengths independently are feasible with only a single metasurface. We also demonstrate the near-field pattern and focusing. Our work opens a new avenue for controlling electromagnetic waves in multi-wavelength application scenarios, which can realize chromatic and achromatic behaviors at will.

2. Principles

The phase modulation mechanisms of metasurfaces mainly consist of two types: propagation phase and geometric phase. The propagation phase is related to wavelength and has nothing to do with the rotation angles of meta-atoms. The opposite is true for the geometric phase. Based on this, we can find six types of pillars whose propagation phase difference at 1064 nm and 1550 nm covers the full range of 2π. The phase difference includes both the propagation phase and the geometric phase. It is worth noting that the geometrical phase is an ideal physical concept. When the resonance effect of a meta-atom at the working wavelength is weaker, the cross-polarization phase is closer to the ideal geometric phase. Conversely, the obtained phase after polarization reversal deviates more from the ideal geometric phase. As shown in Fig. 2(a), this is the diagram of unit structure we adopt. The period is 450 nm, and the substrate is silica, on which are amorphous silicon (a-Si) pillars with a height of 800 nm. In this paper, commercial FDTD software (Lumerical FDTD solutions) is used to obtain the transmission function of meta-atoms. The rectangular a-Si pillar sits on the fused-silica substrate. Periodic boundary conditions are applied along the x and y directions, and perfectly matched layer (PML) conditions are set in the z direction. By varying the length and width, the propagation phase provided by a Si pillar can be changed. The geometrical phase provided by a Si pillar can be changed by varying the rotation angle. The total phase difference between 1064 nm and 1550 nm varying with the length and width of a Si pillar is shown in Fig. 2(b). To achieve full coverage of phase difference within the range of 2π, we selected six types of pillars, as shown in Fig. 2(b) marked S1–S6. In determining the pillars that meet the requirements, we make a trade-off between phase difference and conversion efficiency. Although many pillars are already near the edge of our scanning range, increasing the period can find better pillars. Increasing the period of the unit structure will enlarge the distance between different structural units, reducing the interference effect.

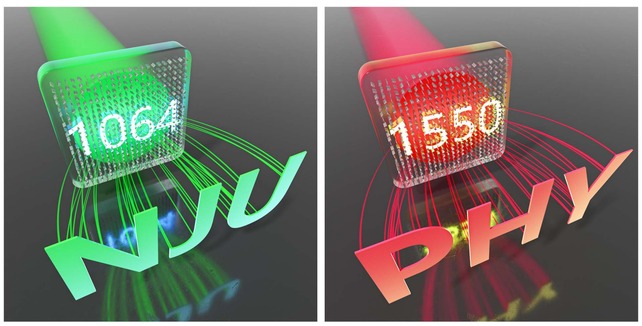

Fig. 1. Schematic of dual-wavelength near- and far-field decoupling metasurfaces.

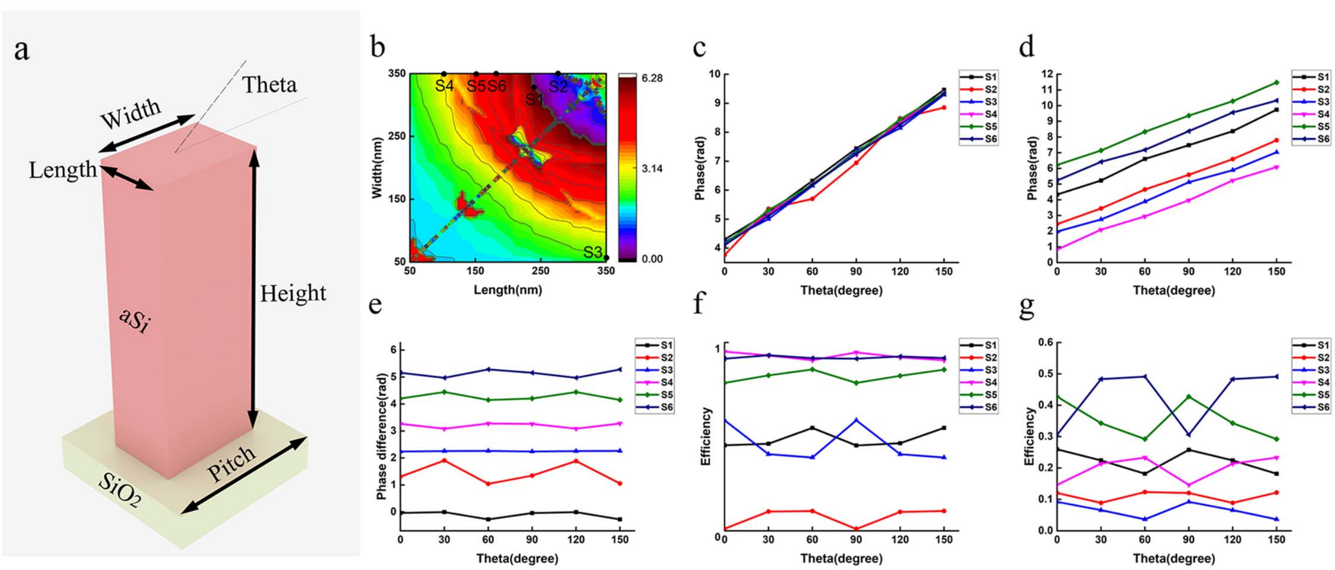

Fig. 2. (a) Structure parameters of a meta-atom. (b) Full-wave simulations varying with width and length. The colormap represents the phase given by a meta-atom. (c) Phase varying with theta for six meta-atoms at the wavelength of 1064 nm. (d) Phase varying with theta for the same six meta-atoms at the wavelength of 1550 nm. (e) Phase difference between 1064 nm and 1550 nm for six meta-atoms. (f) Cross-polarization conversion efficiency for six meta-atoms at the wavelength of 1064 nm. (g) Cross-polarization conversion efficiency for the same six meta-atoms at the wavelength of 1550 nm.

Moreover, the pillars that have been found can display the desired effect. As shown in Fig. 2(c), for the light with an incident wavelength of 1064 nm, the phases of these six pillars are the same and have a good linear relationship with the rotation angle. As shown in Fig. 2(d), for the light with an incident wavelength of 1550 nm, the phases of these six pillars not only have a linear relationship with the rotation angle but also can fully cover the full range of 2π at each rotation angle. The phase difference between two incident wavelengths of the six pillars is shown in Fig. 2(e). There are 36 phase combinations that have been obtained, which can achieve arbitrary and independent phase regulation of incident wavelengths of 1064 nm and 1550 nm. It is worth noting that the S2 structure in Fig. 2(e) has a significantly greater phase difference fluctuation varying with the rotation angle than S1, which is the influence of the resonance effect mentioned above. Figures 2(f) and 2(g) show the polarization conversion efficiency of the six structures at two incident wavelengths. Unfortunately, the transformation efficiency of the S2 structure is very low at both wavelengths, which can also explain the reason for the large fluctuation of phase difference. If the height of the Si pillar continues to increase, better conditions can be found.

Although the amplitude and phase of incident light can be separately controlled by metasurfaces easily, it is difficult to simultaneously control the amplitude and phase of incident light by a single meta-atom. According to the principle of interference, the phase and amplitude of incident light in a super-pixel can be manipulated at the same time as required when only the phases of constituent meta-atoms are demanded. As shown in Fig. 3(a), two groups of meta-atoms are placed across each other. For a single meta-atom, the output electric field in the scalar form is $E_0\xi_{jk}e^{i\phi_{jk}}$, where E_0 is the amplitude of the incident electric field, i is the imaginary number, $j = 1, 2$ is the meta-atom index, $k = \alpha, \beta$ is the polarization basis, the real number ξ_{jk} represents the cross-polarization conversion coefficient of the j meta-atom under the incidence of k polarization basis, and ϕ_{jk} represents the cross-polarization phase of the j meta-atom under the incidence of the k polarization basis. When α polarization comes in, the β polarization comes out ($\langle\alpha|\beta\rangle = 0$). The super-pixel's electric-field amplitude provided by both meta-atoms is

$$\begin{aligned} E_{\mathrm{out},\beta} &= E_0\xi_{1\beta}e^{i\phi_{1\beta}} + E_0\xi_{2\beta}e^{i\phi_{2\beta}} \\ &= E_0 e^{i\frac{\phi_{1\beta}+\phi_{2\beta}}{2}}\left[(\xi_{1\beta}+\xi_{2\beta})\cos\left(\frac{\phi_{1\beta}-\phi_{2\beta}}{2}\right)\right. \\ &\quad \left. + i(\xi_{1\beta}-\xi_{2\beta})\sin\left(\frac{\phi_{1\beta}-\phi_{2\beta}}{2}\right)\right], \end{aligned} \tag{1}$$

$$\begin{aligned} I_{\mathrm{out},\beta} = E_0^2\Bigg[&(\xi_{1\beta}+\xi_{2\beta})^2\cos^2\left(\frac{\phi_{1\beta}-\phi_{2\beta}}{2}\right) \\ &+ (\xi_{1\beta}-\xi_{2\beta})^2\sin^2\left(\frac{\phi_{1\beta}-\phi_{2\beta}}{2}\right)\Bigg]. \end{aligned} \tag{2}$$

When $\phi_{1\beta} - \phi_{2\beta} = 0$,

$$E_{\mathrm{out},\beta} = E_0 e^{i\frac{\phi_{1\beta}+\phi_{2\beta}}{2}}(\xi_{1\beta} + \xi_{2\beta}). \tag{3}$$

When $\phi_{1\beta} - \phi_{2\beta} = \pi$,

$$E_{\mathrm{out},\beta} = iE_0 e^{i\frac{\phi_{1\beta}+\phi_{2\beta}}{2}}(\xi_{1\beta} - \xi_{2\beta}). \tag{4}$$

When $\phi_{1\beta} - \phi_{2\beta} = 0, \pi$, the sum of phases of two pillars determines the phase of the super-pixel. The phase can be manipulated independently and freely when the amplitude intensity is binary coded. The amplitude intensity visibility is defined as

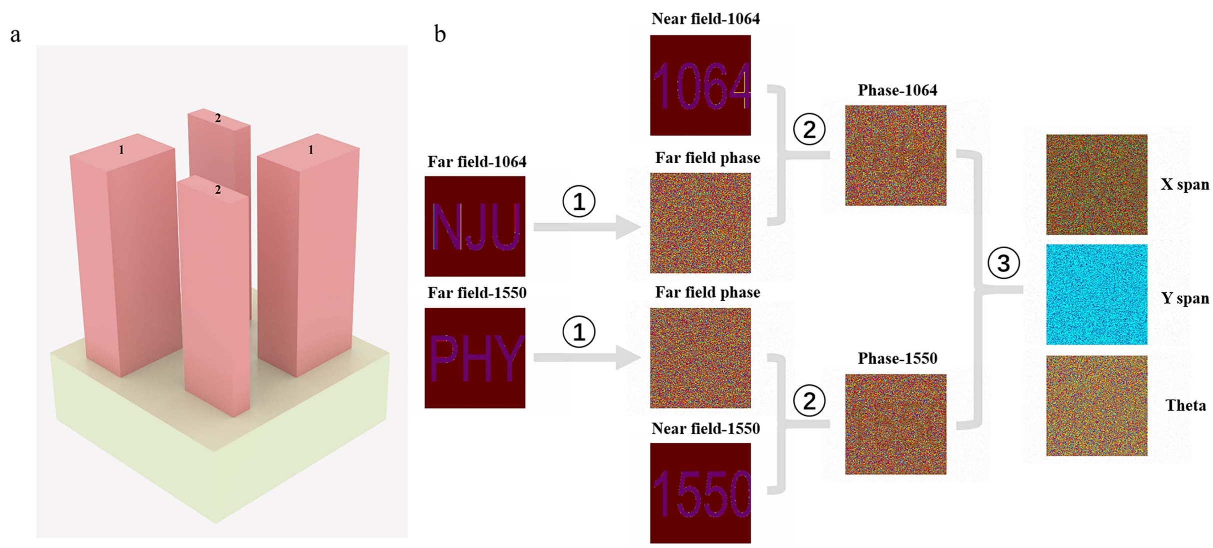

Fig. 3. (a) Meta-atom arrangement of 2×2 at a super-pixel. The 1 and 2 possess different structural parameters. (b) The design process of dual-wavelength near- and far-field decoupling metasurfaces. The ① represents the GS algorithm, ② represents one-to-four algorithm, and ③ represents getting structural parameters from dual-wavelength phase distribution.

$$V = \frac{I_{\text{out},\beta,\max} - I_{\text{out},\beta,\min}}{I_{\text{out},\beta,\max} + I_{\text{out},\beta,\min}} = \frac{2\xi_{1\beta}\xi_{2\beta}}{\xi_{1\beta}^2 + \xi_{2\beta}^2}. \tag{5}$$

Then, we can conclude that to achieve utmost visibility the cross-polarization conversion efficiency is not necessarily equal to unity but needed to be the same. This relaxes the constrains for the pillars.

The design process is shown in Fig. 3(b). Firstly, the patterns of two wavelengths in the near field and far field are determined, respectively, and the far-field patterns are inverted by the Gerchberg–Saxton (GS) algorithm to get the near-field phase, as shown by ① in Fig. 3(b). After obtaining the near-field phase and intensity of the super-pixel, the one-to-four algorithm is designed based on the formula above: the intensity and phase of one super-pixel can be achieved by four pixels. Finally, after the phase distributions of wavelengths of 1064 nm and 1550 nm are obtained, the corresponding phase requirements are realized by using the found meta-atoms, which determine the length, width, and rotation angle distribution of the metasurface.

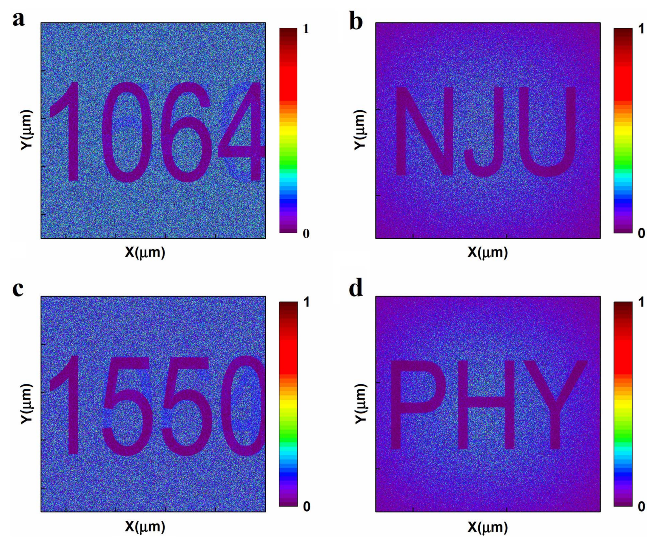

Fig. 4. Simulation results. (a), (c) Near-field intensity distribution at the distance of 100 nm after the metasurface for 1064 nm and 1550 nm, respectively. (b), (d) Far-field intensity distribution after the metasurface for 1064 nm and 1550 nm, respectively.

3. Simulation Results

3.1. Near-field pattern and far-field pattern

The size of the metasurface is $590.4\,\mu\text{m} \times 787.5\,\mu\text{m}$, so it is impossible to use FDTD or other commercial simulation software to calculate the near- and far-field electric-field distribution of the metasurface. We fill the true phase and transmittance of the pillars into each pixel, then put the real transmission function into MATLAB, and finally use the angular spectrum for simulation, which can quickly and accurately simulate the manipulation of the metasurface to the light field. Figures 4(a) and 4(c) show the near-field intensity distribution of the electric field at a distance of 100 nm away from the metasurface, which the light with the incident wavelength of 1064 nm or 1550 nm passes through, respectively. Figures 4(b) and 4(d) show the Fourier hologram of the phase for the incident wavelengths of 1064 nm and 1550 nm, respectively. The phase plane is the same as the near-field observation plane. The target patterns are the same as our designs. It is worth noting that the dual-wavelength near-field intensity distribution has certain crosstalk due to the low polarization conversion efficiency of the structure. This also indirectly proves the accuracy of our simulation algorithm. The crosstalk effect can be reduced if pillars with higher aspect ratio can be prepared. In addition, there is no obvious crosstalk effect in the dual-wavelength far-field intensity distribution. As predicted by the theory above, when the near-field intensity representation takes a binary step, the conversion efficiency does not affect the phase value of the super-pixel. The far-field electric-field distribution is the Fourier transform of the near-field electric-field distribution. According to the convolution theorem, the far-field electric-field distribution is the convolution of the Fourier transform of the near-field electric-field amplitude distribution and phase distribution. The former can be approximated as a delta function, and the convolution of a delta function with the Fourier transform of the near-field electric-field phase distribution is equal to the Fourier transform of the near-field electric-field phase distribution itself, so the crosstalk of the dual-wavelength near-field intensity distribution is not delivered to the dual-wavelength far-field intensity distribution. The working wavelengths used in this work are 1064 nm and 1550 nm. If two closer working wavelengths are chosen, the propagation phase difference between two wavelengths is smaller. It is more difficult to achieve arbitrary independent regulation of dual-wavelength phase, unless the resonance effect is introduced. In addition, choosing a shorter wavelength would make the result worse, because each pixel is equivalent to a small hole; the shorter the working wavelength, the less obvious the diffraction effect, thus reducing the interference effect between pixels.

3.2. Near-field pattern and focusing

Based on the same principle, we can also design dual-wavelength near-field patterns and arbitrary independent focal lengths. Figures 5(a) and 5(d) show the intensity distribution of the near-field electric field at a distance of 100 nm away from the metasurface, which the light with the incident wavelength of 1064 nm or 1550 nm passes through, respectively. Figures 5(b) and 5(c), respectively, show the focusing effect along with the $x-z$ and $y-z$ cross-section planes of the metasurface when the incident wavelength is 1064 nm. Figures 5(e) and 5(f), respectively, show the focusing effect along with the $x-z$ and $y-z$ cross-section planes of the metasurface when the incident wavelength is 1550 nm. From the graph, we can see that the focusing effects in the $x-z$ and $y-z$ cross-section planes are very good, and the modulation of near-field intensity does not affect the focusing. Interestingly, the initial input focal

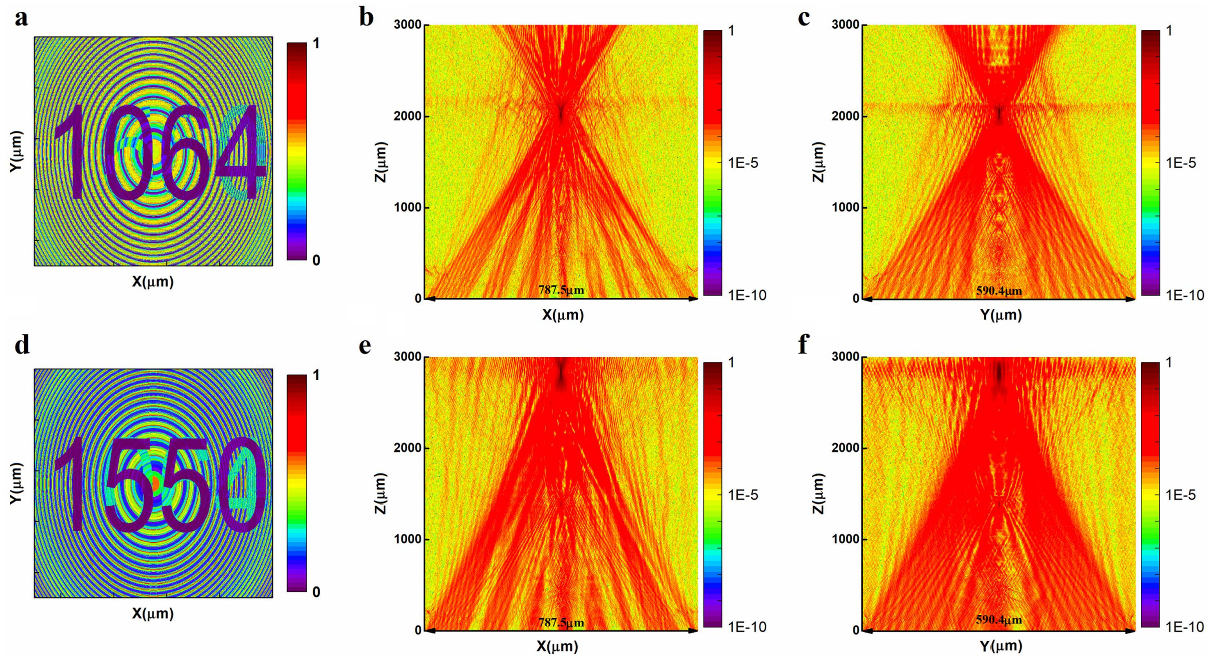

Fig. 5. Simulation results. (a), (d) Near-field intensity distribution at the distance of 100 nm after the metasurface for 1064 nm and 1550 nm, respectively. (b), (c) Verification of the converging metalens at an incident wavelength of 1064 nm for horizontal and vertical directions, respectively. (e), (f) Verification of the converging metalens at an incident wavelength of 1550 nm for horizontal and vertical directions, respectively.

lengths of 1064 nm and 1550 nm are 500 μm and 700 μm, respectively, but it can be seen from Fig. 5 that the final output focal lengths of 1064 nm and 1550 nm are about 2000 μm and 2800 μm, respectively, which are caused by the design principle. The initial input focal length is f, the final output focal length is f', and the distance from a point on the sample to the origin is r. When a pixel is represented by a super-pixel consisting of four pixels, r is twice as large as before, namely,

$$-\frac{2\pi}{\lambda}\left(\sqrt{r^2+f^2}-f\right)=-\frac{2\pi}{\lambda}\left(\sqrt{4r^2+f'^2}-f'\right), \quad (6)$$

when $f, f' > r$,

$$f' = 4f. \quad (7)$$

The above equations suggest that when the NA of the lens is very small, the final output focal length is four times as large as the initial input focal length.

Metasurfaces are wavelength-dependent structures. Using this method, it is easy to design dual-wavelength planar devices with the same or different focal lengths, and there is no need to find wavelength-selective structures in segmented implementation. As shown in Fig. 6(a), each data point represents the situation in which one wavelength is fixed at one initial input focal length, and the initial input focal length of the other wavelength changes from 10 μm to 300 μm. When the initial input focal length of 1064 nm is 10–150 μm, the change of the initial focal length of 1550 nm has a great influence on the final output focal length of 1064 nm, and the relationship between the final

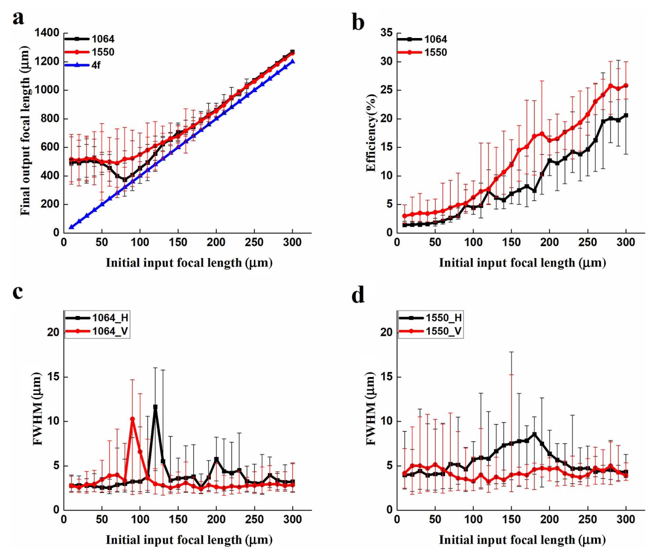

Fig. 6. Simulation results. (a) The relationships between final output focus length and initial input focus length. (b) The average efficiency of focusing obtained for 1064 nm and 1550 nm. (c), (d) The FWHMs obtained for horizontal and vertical polarizations for 1064 nm and 1550 nm, respectively. The error bars represent the minimum and maximum values.

output focal length and the initial input focal length for 1064 nm is not four-fold linear. Otherwise, when the initial input focal length of 1064 nm is 150–300 μm, the initial input focal length of 1550 nm has less influence on the final output focal length of 1064 nm, and the final output focal length of 1064 nm is closer to a four-fold relationship with the initial input focal length of 1550 nm. The case is the same when the 1550 nm initial input focal length is unchanged, while the 1064 nm initial input focal length varies. In addition to focusing, the far-field function can also be beam deflection, and the final output deflection angle should be 1/2 as large as the initial design deflection angle. In order to better characterize the focusing performance, Fig. 6(b) shows the focusing efficiency for two wavelengths. The longer the focal length, the higher the focusing efficiency. Figures 6(c) and 6(d) show the sizes of the focusing spot in the $x-z$ and $y-z$ cross-section planes for two wavelengths, respectively. The size range of the minimum focusing spot is 1.5λ–2λ, which is close to the diffraction limit. However, in other cases, the focused spot does not reach the diffraction limit, which is not caused by the near-field intensity modulation, because the near-field intensity pattern does not change, but by the efficiency of the selected meta-atom units. This problem can be solved by selecting pillars with a higher aspect ratio.

4. Discussion

In summary, we show that we can use the different dispersion properties of propagation phase and geometric phase of metasurfaces to achieve complete decoupling of dual-wavelength regulation in terms of phase and intensity. Firstly, we find the pillars whose two-wavelength propagation phase difference covers 2π. Then, using the non-dispersive property of geometric phase, we can realize dual-wavelength arbitrary and independent regulation of phase only by rotation angle. Combining with the principle of interference, we introduce the design process in detail to realize the decoupling of near-field and far-field functions. Near-field patterns and far-field holographic patterns have been successfully demonstrated. Crosstalk exists between dual-wavelength near-field patterns, which can be effectively solved if pillars with a higher aspect ratio are used. In addition, the far-field holographic function can be replaced by focusing. According to our theoretical analysis, when the NA of the lens is small, the final output focal length is four times as large as the initial input focal length. The simulation results are in good agreement with theoretical analysis. The proposed method can adjust the focal length of two wavelengths to be equal or different arbitrarily and has great design flexibility for different applications. Moreover, the proposed method can be easily extended to dual-wavelength decoupling of near-field and far-field functions for different polarizations: for example, using the decoupling of horizontal and vertical polarizations in propagation phase or one operating wavelength using only propagation phase, and the other wavelength using geometric phase plus propagation phase.

The theoretical design provided in this paper can be fully realized experimentally. The highest aspect ratio of the adopted meta-atoms is roughly 8:1, which lies within a reasonable range. Via plasma-enhanced chemical vapour deposition (PECVD), electron beam lithography (EBL), inductively coupled plasma and reactive ion etching (ICP-RIE) etcher, and so on, a complete set of micro/nano fabrication processes makes sample fabrication possible. To the best of our knowledge, this is the first time that simultaneous complete near- and far-field decoupling for two wavelengths is demonstrated. This functionality can not only improve the information density and security of nanostructured metasurfaces, but also stands a good chance of broadening application scenarios such as AR applications and stimulated emission depletion microscopy, in which multi-wavelength capability is necessary. This work is instructive for achieving more sophisticated multi-wavelength and multi-functional meta-devices and realizing useful applications in practical systems.

Acknowledgement

This work was supported by the National Key Research and Development Program of China (No. 2017YFA0303700), National Natural Science Foundation of China (Nos. 11621091, 11822406, 11834007, 11774164, and 11774162), and Fundamental Research Funds for the Central Universities (No. 020414380175).

References

1. N. Yu, P. Genevet, A. Kats Mikhail, F. Aieta, J.-P. Tetienne, F. Capasso, and Z. Gaburro, “Light propagation with phase discontinuities: generalized laws of reflection and refraction,” Science **334**, 333 (2011).
2. X. Ni, J. Wong Zi, M. Mrejen, Y. Wang, and X. Zhang, “An ultrathin invisibility skin cloak for visible light,” Science **349**, 1310 (2015).
3. S. Wang, P. C. Wu, V.-C. Su, Y.-C. Lai, C. H. Chu, J.-W. Chen, S.-H. Lu, J. Chen, B. Xu, and C.-H. Kuan, “Broadband achromatic optical metasurface devices,” Nat. Commun. **8**, 187 (2017).
4. S. Wang, P. C. Wu, V.-C. Su, Y.-C. Lai, M.-K. Chen, H. Y. Kuo, B. H. Chen, Y. H. Chen, T.-T. Huang, and J.-H. Wang, “A broadband achromatic metalens in the visible,” Nat. Nanotechnol. **13**, 227 (2018).
5. G. Zheng, H. Mühlenbernd, M. Kenney, G. Li, T. Zentgraf, and S. Zhang, “Metasurface holograms reaching 80% efficiency,” Nat. Nanotechnol. **10**, 308 (2015).
6. W. Klein Matthias, C. Enkrich, M. Wegener, and S. Linden, “Second-harmonic generation from magnetic metamaterials,” Science **313**, 502 (2006).
7. L. Li, Z. Liu, X. Ren, S. Wang, V. C. Su, M. K. Chen, C. H. Chu, H. Y. Kuo, B. Liu, W. Zang, G. Guo, L. Zhang, Z. Wang, S. Zhu, and D. P. Tsai, “Metalens-array-based high-dimensional and multiphoton quantum source,” Science **368**, 1487 (2020).
8. T. Stav, A. Faerman, E. Maguid, D. Oren, V. Kleiner, E. Hasman, and M. Segev, “Quantum entanglement of the spin and orbital angular momentum of photons using metamaterials,” Science **361**, 1101 (2018).
9. K. Wang, J. G. Titchener, S. S. Kruk, L. Xu, H. P. Chung, M. Parry, I. I. Kravchenko, Y. H. Chen, A. S. Solntsev, Y. S. Kivshar, D. N. Neshev, and A. A. Sukhorukov, “Quantum metasurface for multiphoton interference and state reconstruction,” Science **361**, 1104 (2018).
10. Q. Li, W. Bao, Z. Nie, Y. Xia, Y. Xue, Y. Wang, S. Yang, and X. Zhang, “A non-unitary metasurface enables continuous control of quantum photon–photon interactions from bosonic to fermionic,” Nat. Photonics **15**, 267 (2021).
11. T. Roger, S. Vezzoli, E. Bolduc, J. Valente, J. J. F. Heitz, J. Jeffers, C. Soci, J. Leach, C. Couteau, N. I. Zheludev, and D. Faccio, “Coherent perfect absorption in deeply subwavelength films in the single-photon regime,” Nat. Commun. **6**, 7031 (2015).
12. L. M. Procopio, L. A. Rozema, Z. J. Wong, D. R. Hamel, K. O’Brien, X. Zhang, B. Dakic, and P. Walther, “Single-photon test of hyper-complex quantum theories using a metamaterial,” Nat. Commun. **8**, 15044 (2017).

13. J. Zhou, S. Liu, H. Qian, Y. Li, H. Luo, S. Wen, Z. Zhou, G. Guo, B. Shi, and Z. Liu, "Metasurface enabled quantum edge detection," Sci. Adv. **6**, eabc4385 (2020).
14. H. Defienne, B. Ndagano, A. Lyons, and D. Faccio, "Polarization entanglement-enabled quantum holography," Nat. Phys. **17**, 591 (2021).
15. P. K. Jha, X. Ni, C. Wu, Y. Wang, and X. Zhang, "Metasurface-enabled remote quantum interference," Phys. Rev. Lett. **115**, 025501 (2015).
16. P. K. Jha, N. Shitrit, J. Kim, X. Ren, Y. Wang, and X. Zhang, "Metasurface-mediated quantum entanglement," ACS Photonics **5**, 971 (2017).
17. P. K. Jha, N. Shitrit, X. Ren, Y. Wang, and X. Zhang, "Spontaneous exciton valley coherence in transition metal dichalcogenide monolayers interfaced with an anisotropic metasurface," Phys. Rev. Lett. **121**, 116102 (2018).
18. A. S. Solntsev, G. S. Agarwal, and Y. S. Kivshar, "Metasurfaces for quantum photonics," Nat. Photonics **15**, 327 (2021).
19. J. Liu, M. Shi, Z. Chen, S. Wang, Z. Wang, and S. Zhu, "Quantum photonics based on metasurfaces," Opto-Electron. Adv. **4**, 09200092 (2021).
20. O. Eisenbach, O. Avayu, R. Ditcovski, and T. Ellenbogen, "Metasurfaces based dual wavelength diffractive lenses," Opt. Express **23**, 3928 (2015).
21. J. Ding, N. Xu, H. Ren, Y. Lin, W. Zhang, and H. Zhang, "Dual-wavelength terahertz metasurfaces with independent phase and amplitude control at each wavelength," Sci. Rep. **6**, 34020 (2016).
22. J. Ding, S. An, B. Zheng, and H. Zhang, "Multiwavelength metasurfaces based on single-layer dual-wavelength meta-atoms: toward complete phase and amplitude modulations at two wavelengths," Adv. Opt. Mater. **5**, 1700079 (2017).
23. Z. Shi, A. Y. Zhu, Z. Li, Y.-W. Huang, W. T. Chen, C.-W. Qiu, and F. Capasso, "Continuous angle-tunable birefringence with freeform metasurfaces for arbitrary polarization conversion," Sci. Adv. **6**, eaba3367 (2020).
24. A. Leitis, A. Tittl, M. Liu, B. H. Lee, M. B. Gu, Y. S. Kivshar, and H. Altug, "Angle-multiplexed all-dielectric metasurfaces for broadband molecular fingerprint retrieval," Sci. Adv. **5**, eaaw2871 (2019).
25. S. M. Kamali, E. Arbabi, A. Arbabi, Y. Horie, M. Faraji-Dana, and A. Faraon, "Angle-multiplexed metasurfaces: encoding independent wavefronts in a single metasurface under different illumination angles," Phys. Rev. X **7**, 041056 (2017).
26. Y.-J. Gao, X. Xiong, Z. Wang, F. Chen, R.-W. Peng, and M. Wang, "Simultaneous generation of arbitrary assembly of polarization states with geometrical-scaling-induced phase modulation," Phys. Rev. X **10**, 031035 (2020).
27. Y. Guo, S. Zhang, M. Pu, Q. He, J. Jin, M. Xu, Y. Zhang, P. Gao, and X. Luo, "Spin-decoupled metasurface for simultaneous detection of spin and orbital angular momenta via momentum transformation," Light Sci. Appl. **10**, 63 (2021).
28. H. Ren, X. Fang, J. Jang, J. Bürger, J. Rho, and S. A. Maier, "Complex-amplitude metasurface-based orbital angular momentum holography in momentum space," Nat. Nanotechnol. **15**, 948 (2020).
29. H. Ren, G. Briere, X. Fang, P. Ni, R. Sawant, S. Héron, S. Chenot, S. Vézian, B. Damilano, and V. Brändli, "Metasurface orbital angular momentum holography," Nat. Commun. **10**, 2986 (2019).
30. M. Liu, W. Zhu, P. Huo, L. Feng, M. Song, C. Zhang, L. Chen, H. J. Lezec, Y. Lu, and A. Agrawal, "Multifunctional metasurfaces enabled by simultaneous and independent control of phase and amplitude for orthogonal polarization states," Light Sci. Appl. **10**, 107 (2021).
31. Q. Fan, M. Liu, C. Zhang, W. Zhu, Y. Wang, P. Lin, F. Yan, L. Chen, H. J. Lezec, and Y. Lu, "Independent amplitude control of arbitrary orthogonal states of polarization via dielectric metasurfaces," Phys. Rev. Lett. **125**, 267402 (2020).
32. J. B. Mueller, N. A. Rubin, R. C. Devlin, B. Groever, and F. Capasso, "Metasurface polarization optics: independent phase control of arbitrary orthogonal states of polarization," Phys. Rev. Lett. **118**, 113901 (2017).
33. H. Wang, Z. Zhang, K. Zhao, W. Liu, P. Wang, and Y. Lu, "Independent phase manipulation of co- and cross-polarizations with all-dielectric metasurface," Chin. Opt. Lett. **19**, 053601 (2021).
34. G. Yoon, J. Kim, J. Mun, D. Lee, K. T. Nam, and J. Rho, "Wavelength-decoupled geometric metasurfaces by arbitrary dispersion control," Commun. Phys. **2**, 129 (2019).